Structural phase diagram of $La_{1-x}Sr_xMnO_{3+\delta}$: Relationship to magnetic and transport properties

J. F. Mitchell,* D. N. Argyriou,† C. D. Potter, D. G. Hinks, J. D. Jorgensen, and S. D. Bader
Materials Science Division, Argonne National Laboratory, Argonne, Illinois 60439
(Received 27 December 1995)

The structural properties of $La_{1-x}Sr_xMnO_{3+\delta}$ have been studied using neutron powder diffraction as a function of both Sr doping ($0 \leqslant x \leqslant 0.225$) and oxygen partial pressure during synthesis [2.1×10^{-4} atm$\leqslant P(O_2) \leqslant 1$ atm]. A structural phase diagram constructed as a function of these parameters has a rhombohedral phase ($R\bar{3}c$), an orthorhombic phase ($Pbnm$), and a monoclinic phase ($P2_1/c$). For a given x, decreasing $P(O_2)$ yields smaller cation vacancy concentrations. At low temperature, the R phase is ferromagnetic, while the M phase is antiferromagnetic. The O phase is ferromagnetic for $x \geqslant 0.125$, and the ferromagnetism is independent of the O-R phase transition that coincides with the transition from nonmetal to metal. Transport measurements made between 20 and 350 K show that O and M samples are nonmetallic ($d\rho/dT<0$), while the R samples exhibit a temperature-dependent nonmetal-to-metal transition at temperatures close to the Curie temperature. Magnetoresistance (MR) is observed in all three phases. The largest value at 9 T, found in the orthorhombic and monoclinic samples, is of similar order ($\Delta\rho=\rho_0-\rho_{9T}\sim10^4\ \Omega$ cm) to that reported for 10^6% colossal MR powder samples. However, our lower sintering temperatures result in large ρ_{9T} values that yield $\Delta\rho/\rho_{9T}\sim230\%$. [S0163-1829(96)05833-X]

I. INTRODUCTION

The observation of ''colossal'' magnetoresistance (CMR) in manganese oxides crystallizing in the perovskite structure has generated considerable interest in the physical properties of this class of compounds, particularly the interplay of structure, magnetism, and electronic transport. Colossal magnetoresistance has been reported for (among others) $La_{1-x}M_xMnO_{3+\delta}$ (M=Sr,Ca,Ba,Pb),[1–6] and $L_{2/3}Sr_{1/3}MnO_3$ (L=Nd,Sm),[7] and a vigorous search for new materials exhibiting this important property is currently underway. While in the undoped compound $LaMnO_{3+\delta}$ ($\delta\sim0$) the Mn ions are formally trivalent (with an electron configuration $t_{2g}^3e_g^1$), lattice defects such as cation vacancies[8] and/or substitution of divalent cations for La^{3+} can dope holes into the e_g levels, resulting in a formally mixed valent Mn^{3+}/Mn^{4+} matrix; these doped holes may be either localized or itinerant. It is believed that the CMR effect is due to a double exchange of electrons between ferromagnetically coupled Mn^{3+} and Mn^{4+} ions,[9,10] and indeed as a general rule the materials have the largest magnetoresistance in the same temperature regime as the onset of ferromagnetic ordering. More recently, Millis, Littlewood, and Shraiman[11] have proposed that the double exchange model alone does not wholly account for CMR in $La_{1-x}Sr_xMnO_{3+\delta}$ and have claimed that a strong electron-phonon interaction arising from the Jahn-Teller splitting of the Mn d levels plays an important role. Pickett and Singh have calculated the local spin-density approximation band structure of $La_{1-x}Ca_xMnO_3$ and claim that metal-oxygen hybridization cannot be ignored.[12] Independent of its importance to the mechanism of CMR, the ferromagnetism in these compounds is apparently strongly coupled to the lattice, as Asamitsu *et al.*[5] have demonstrated in $La_{0.825}Sr_{0.175}MnO_3$ by inducing an orthorhombic to rhombohedral structural phase transition with an applied magnetic field.

Recent transport measurements by Urushibara *et al.*[4] on $La_{1-x}Sr_xMnO_3$ single crystals demonstrate that samples with small levels of Sr doping ($x<0.15$) are nonmetallic even at low temperature, while those with higher Sr doping ($x>0.15$) are metallic at low temperature. These latter samples exhibit a metal-insulator transition close to the Curie temperature T_C. Urushibara reports the largest magnetoresistance effect was observed for samples with $x\leqslant0.175$. For higher Sr doping levels, the MR decreases significantly as the samples become metallic.

Much attention has been paid to the undoped compound $LaMnO_{3+\delta}$. Van Roosmalen and co-workers[8,13–15] have demonstrated from neutron powder diffraction and density measurements that vacancies occur on both the rare-earth and transition-metal sites in $LaMnO_{3+\delta}$, but that the oxygen sublattice is fully occupied for this compound. The same workers found no evidence for interstitial oxygen. They have also shown that similar considerations apply for the Sr-doped lanthanum manganite. The consensus in the literature is that for high cation vacancy concentrations, $LaMnO_{3+\delta}$ crystallizes in a rhombohedral structure ($R\bar{3}c$), while for less cation-defective compositions an orthorhombic structure ($Pbnm$) is observed.[15,16] In addition, Yakel[17] has reported a monoclinic phase for stoichiometric $LaMnO_{3.0}$. A number of detailed investigations have been completed on the relationship between crystal chemistry and structure in $LaMnO_{3+\delta}$. Jonker and van Santen[18] and Wold and Arnott[19] independently showed that the synthesis temperature and $P(O_2)$ can be used to control the Mn^{4+}/Mn^{3+} ratio; high synthesis temperatures ($\sim$1350 °C) and/or reducing atmospheres produce samples with small concentrations of Mn^{4+}, while lower temperatures ($\sim$1100 °C) and/or oxidizing atmospheres result in significant concentrations of Mn^{4+}.

Important questions exist about the mechanism of the CMR in the perovskite manganese oxides. Crucial to both a theoretical and experimental understanding of this phenom-

enon is a detailed picture of the structural phase diagram, its dependence on synthesis conditions and composition, the structural parameters (bond lengths, angles) for the various phases, and the nature and concentration of defects. In this paper we report the structural, magnetic, and transport properties of a series of $La_{1-x}Sr_xMnO_{3+\delta}$ samples ($0 \leqslant x \leqslant 0.225$) prepared at 1000 °C under a range of oxygen partial pressures, 2.1×10^{-4} atm$\leqslant P(O_2) \leqslant 1$ atm. We map the structural phase diagram versus x and $P(O_2)$, identifying three structural polymorphs: rhombohedral ($R\bar{3}c$), orthorhombic ($Pbnm$), and monoclinic ($P2_1/c$), the last of which has not previously been described in detail. Magnetic measurements show that the rhombohedral samples become ferromagnets for $x \geqslant 0.125$ and that T_C is sensitive to both Sr doping, x, and $P(O_2)$. The latter is in distinct contrast with work reported on the related $(La,Ca)MnO_{3+\delta}$ system.[20] An antiferromagnetic ground state is observed for the monoclinic phase. The orthorhombic phase is known to be antiferromagnetic for $0 \leqslant x < 0.1$ and ferromagnetic for $x > 0.1$.[4] We verify that ferromagnetism is independent of crystal symmetry for $x \geqslant 0.125$. Transport measurements on a range of samples indicate that both orthorhombic and monoclinic samples are nonmetallic throughout the temperature range 20 K$<T<$350 K and that the rhombohedral samples undergo a metal-to-insulator transition at a temperature close to T_C, consistent with the double exchange model of transport.

II. SAMPLE PREPARATION AND EXPERIMENTAL PROCEDURE

The $La_{1-x}Sr_xMnO_{3+\delta}$ series was synthesized by coprecipitation of insoluble carbonates from a solution of the corresponding nitrates. Starting materials consisted of the high-purity oxides La_2O_3 (Johnson-Matthey REacton, 99.99%) and MnO_2 (Johnson-Matthey Puratronic, 99.999%); $SrCO_3$ (Johnson-Matthey Puratronic, 99.999%) was used as a Sr source. La_2O_3 was prefired in flowing oxygen at 1000 °C for several hours to decompose residual carbonates, and the MnO_2 was treated in flowing oxygen at 425 °C and slowly cooled (1 °C/min) to room temperature. $SrCO_3$ was used as received. Prefired MnO_2 was dissolved in concentrated HCl and the solution was slowly evaporated to dryness. The residue was then redissolved in a minimum of H_2O. To remove chlorides, concentrated HNO_3 was added to the solution, which was again heated to dryness. The resulting pink solid was dissolved in H_2O. In a separate flask, concentrated nitric acid was slowly added to a stoichiometric mixture of $SrCO_3$ and the prefired La_2O_3. This solution was then added to the manganese solution and the cations coprecipitated by slow addition of a saturated $(NH_4)_2CO_3$ solution. Precipitation is complete when the supernatant is slightly basic (pH$\sim$7–8). The supernatant was then decanted and the precipitate dried and pulverized to yield a fine, light pink precursor powder. The precursor powder was slowly heated (0.5 °C/min) in flowing oxygen to 250 °C to remove water. The temperature was then ramped at 10 °C/min to 1000 °C and held at this temperature for 10 h before rapidly cooling to room temperature. The resulting material is an extremely fine black powder. Subsequent annealing under various $P(O_2)$ (O_2/Ar mixtures) followed the same schedule: 10 °C/min to 1000 °C, 10 h at temperature, and rapid cool to room temperature in the synthesis atmosphere. Using this procedure, $La_{[1]-x}Sr_xMnO_{3+\delta}$ samples were synthesized with $x=0.0$, 0.025, 0.075, 0.125, 0.175, and 0.225 under $P(O_2)$ of 1.0, 0.194, 9.1×10^{-3}, 1.0×10^{-3}, and 2.1×10^{-4} atm for each Sr composition.

Neutron-diffraction patterns were measured from all $La_{1-x}Sr_xMnO_{3+\delta}$ samples using the special environment powder diffractometer at Argonne's Intense Pulsed Neutron Source.[21] For room-temperature measurements, the samples were placed in vanadium cans. Data were collected on all detector banks, but only the higher resolution backscattering data ($\Delta d/d=0.035$) were analyzed. Diffraction patterns were analyzed by the Rietveld method using the program GSAS.[22] In these refinements, data were analyzed over the d-spacing range of 0.5–4 Å. The background was modeled using an eight-term cosine Fourier series, and diffraction peaks were described using a two-sided exponential that was convoluted with a Gaussian and a Lorentzian to describe the instrumental and sample contribution to the peak profile, respectively. Atom positions, temperature factors, and the occupancies of both cation sites were refined. Certain samples contained two polymorphs of $La_{1-x}Sr_xMnO_{3+\delta}$. In these cases site occupancies were not refined. For Sr-doped samples the La/Sr ratio was fixed to that of the starting composition, and an overall occupancy for the site was refined.

Measurements of both the susceptibility and magnetization were performed in a Quantum Design PPMS 6000 system. For resistivity measurements, pressed pellets of $La_{1-x}Sr_xMnO_{3+\delta}$ were cut into rectangular bars ($\sim 2\times2\times8$ mm^3) and mounted on Corning Glass cover slides. Four wire leads were attached with silver paint; extra silver paint was used at the ends of the bar to improve thermal contact. The resistance was measured with a bridge using dc currents in the range 1 μA to 0.5 mA. The sample resistance ranged from 0.5 Ω (in the metallic regime) up to several MΩ for the nonmetallic samples at low temperature. The magnetoresistance was measured with an applied field of 9 T and is defined as $(\rho_0-\rho_{9T})/\rho_{9T}$ where ρ_0 and ρ_{9T} are the resistance in zero field and applied field, respectively. Each sample was subjected to several cycles in both temperature and field to insure that the measured resistance was not hysteretic. Care was taken to insure that measurements were made in the Ohmic regime of the samples. Selected samples were measured using the van der Pauw method[23] to ascertain absolute resistivities.

III. STRUCTURAL PHASE DIAGRAM AND DEFECT CHEMISTRY

Neutron-diffraction patterns measured from samples prepared for this study reveal three distinct structural phases at room temperature: rhombohedral (R), space group $R\bar{3}c$, orthorhombic (O), space group $Pbnm$, and monoclinic (M), space group $P2_1/c$. From this information we construct the structural phase diagram of $La_{1-x}Sr_xMnO_{3+\delta}$ shown in Fig. 1 as a function of x and $P(O_2)$. Open circles in Fig. 1 denote mixed-phase samples with approximately equal amounts of the R and O phase. For the purposes of this work, these samples delineate the rhombohedral-orthorhombic phase boundary. In contrast, no mixtures of O and M phase were observed in our samples. We find that the R phase occurs in

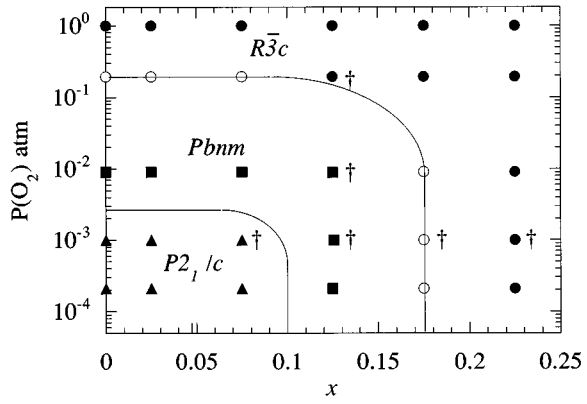

FIG. 1. Structural phase diagram of $La_{1-x}Sr_xMnO_{3+\delta}$ as a function of Sr doping x and $P(O_2)$. R phase (●); O phase (■); M phase (▲). Mixed R- and O-phase samples (○). Samples chosen for transport measurements are marked by a †.

the extreme regions of the phase diagram, bounded by the region $0 \leqslant x \leqslant 0.175$, 0.195 atm$<P(O_2)<$1.0 atm, and at all measured $P(O_2)$ for $0.175<x<0.225$. For low $P(O_2)$ values (2.1×10^{-4} atm$<P(O_2)<1.0\times10^{-3}$ atm) and small Sr-doping levels ($0 \leqslant x \leqslant 0.075$), the monoclinic ($M$) phase is stable. This latter result is consistent with the work Jonker and van Santen[18] and Wold and Arnott[19] for undoped samples synthesized under reducing conditions. As shown in Fig. 1, the O phase is found in the region between the rhombohedral and monoclinic stability fields. Representative Rietveld fits to the data for all three phases are shown in Fig. 2. Table I lists the lattice parameters measured from all samples, and structural parameters are given in Tables II–IV.

We have also investigated a portion of the low-temperature phase diagram of $La_{1-x}Sr_xMnO_{3+\delta}$ by measuring neutron powder-diffraction patterns of selected samples at 20 K. We find that the low-temperature phase diagram is essentially the same as the one observed at room temperature with the exception of certain rhombohedral samples lying close to the R-O phase boundary; these samples [$x=0.125$, 0.175; $P(O_2)=0.195$ atm] transformed to the O phase on cooling.

In the rhombohedral structure, the Mn ion is located at the center of a nearly regular octahedron with O atoms at each vertex, as shown in Fig. 3(a). All Mn-O bonds are the same length. Refined values for the O-Mn-O angles reveal that the axes of the MnO_6 octahedron are slightly distorted from 90°, the maximum distortion being approximately 1°. Neighboring MnO_6 octahedra share vertices to form a three-dimensional network, while La and Sr are randomly distributed over equivalent 12-fold coordinated sites, at the center of eight MnO_6 octahedra. Unlike the parent cubic perovskite structure, the MnO_6 octahedra in the rhombohedral structure are tilted along the $[110]_c$ cubic direction; the O-Mn-O angle is ~163°. According to existing theories of MR, the critical structural parameters affecting magnetism and transport are the Mn-O-Mn tilt angle between linked octahedra and the Mn-O distance.[10,11] It is thought that these parameters control the electronic hopping matrix element and hence affect the transport characteristics of the material. Table V(a) lists bond lengths and angles for the R phase. As can be seen

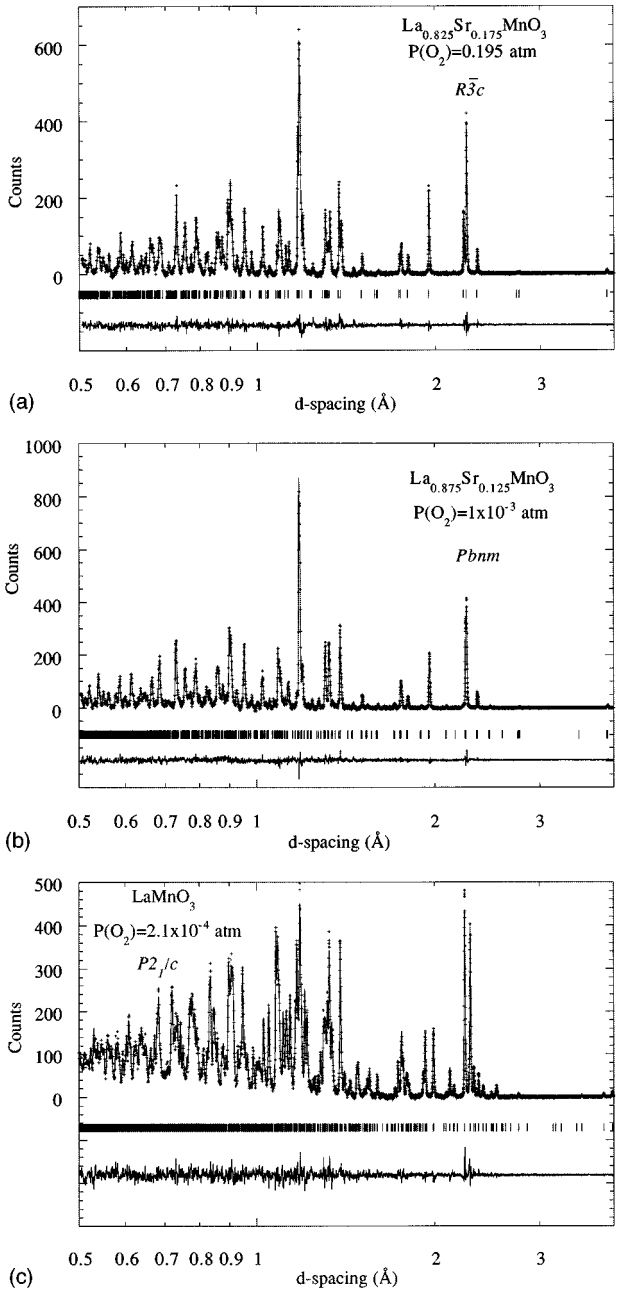

FIG. 2. Observed (+) and fitted (continuous line) neutron-diffraction pattern measured from (a) rhombohedral, (b) orthorhombic, and (c) monoclinic samples at room temperature. The difference between the observed and fitted patterns is displayed at the bottom of each figure. The expected reflection positions are marked underneath the diffraction pattern. The background has been subtracted. The small peak visible at $d=1.45$ Å is due to Al from the sample holder.

from this table, these metrical parameters are relatively insensitive to Sr doping.

In the O phase [synthesized under conditions of reduced $P(O_2)$, see Fig. 1], the MnO_6 octahedra are irregular, and the rhombohedral-to-orthorhombic phase transition can be understood as a cooperative Jahn-Teller distortion of these octahedra. The Jahn-Teller distortion of an MnO_6 octahedron arises as a consequence of the orbitally degenerate electronic state of the Mn^{3+} ion in an octahedral crystal field. For a

TABLE I. Lattice parameters for the *R*, *O*, and *M* phases as a function of Sr doping, *x*, and $P(O_2)$. In the cases where mixed phases of *R* and *O* were observed in the sample, both sets of lattice parameters are given.

x	*a* (Å)	*b* (Å)	*c* (Å)	β (°)
$P(O_2)=1$ atm				
0.0	5.5245(1)		13.3446(1)	
0.025	5.5273(1)		13.3375(2)	
0.075	5.5280(1)		13.3474(1)	
0.125	5.5246(1)		13.3510(2)	
0.175	5.5181(1)		13.3554(3)(2)	
0.225	5.5165(1)		13.3626(3)	
$P(O_2)=0.195$ atm				
0.0	5.5347(2)		13.3521(3)	
	5.5351(2)	5.4995(2)	7.7906(4)	
0.025	5.5356(2)		13.3552(4)	
	5.5362(2)	5.4969(2)	7.7870(3)	
0.075	5.5363(2)		13.3516(5)	
	5.5384(2)	5.4961(2)	7.7833(3)	
0.125	5.5340(1)		13.3614(2)	
0.175	5.5291(1)		13.3644(3)	
0.225	5.5242(1)		13.3691(2)	
$P(O_2)=9.1\times10^{-3}$ atm				
0.0	5.5414(2)	5.5827(2)	7.7557(3)	
0.025	5.5392(2)	5.5828(2)	7.7594(3)	
0.075	5.5422(2)	5.5590(2)	7.7710(2)	
0.125	5.5420(1)	5.5090(1)	7.7931(1)	
0.175	5.5352(1)		13.3717(2)	
	5.5418(3)	5.5056(2)	7.7888(4)	
0.225	5.2167(4)		13.3651(2)	
$P(O_2)=1.0\times10^{-3}$ atm				
0.0	7.9416(5)	7.7112(2)	7.9310(5)	91.480(2)
0.025	7.9109(7)	7.7220(3)	7.9244(8)	91.159(2)
0.075	7.8780(4)	7.7412(2)	7.8943(4)	90.620(2)
0.125	5.5404(1)	5.5184(1)	7.7942(2)	
0.175	5.5338(3)		13.3695(7)	
	5.5434(4)	5.5105(3)	7.7858(6)	
0.225	5.5226(4)		13.3666(2)	
$P(O_2)=2.1\times10^{-4}$ atm				
0.0	7.9670(5)	7.7000(2)	7.9564(5)	91.884(2)
0.025	7.9425(5)	7.7154(2)	7.9262(5)	91.399(2)
0.075	7.8767(4)	7.7376(2)	7.8976(4)	90.681(2)
0.125	5.5374(4)	5.5236(3)	7.7842(3)	
0.175	5.5234(4)		13.3721(7)	
	5.5412(9)	5.5358(9)	7.779(1)	
0.225	5.5250(1)		13.3851(3)	

fixed temperature, a lower $P(O_2)$ during synthesis leads to a greater Mn^{3+} concentration in the sample (*vide infra*). As the Mn^{3+}/Mn^{4+} ratio increases, the electronic energy gained by removing the electronic degeneracy eventually outweighs the elastic forces opposing distortion of the octahedral network, and a cooperative distortion of the octahedral network ensues. The result of such a cooperative Jahn-Teller distortion is the orthorhombic phase of $La_{1-x}Sr_xMnO_{3+\delta}$. The distorted octahedron has three different Mn-O distances, one between Mn and axial oxygens (O_a) and two between Mn and the equatorial oxygens (O_e). Because of the cooperative nature of the distortion of the MnO_6 octahedra, two octahedral tilt angles result: Mn-O_a-Mn along the *c* axis and Mn-O_e-Mn in the *a*-*b* plane. The La atom is also displaced from its ideal site along the $[100]_c$ direction. A section of the orthorhombic structure of $La_{0.875}Sr_{0.125}MnO_{3+\delta}$ is shown in Fig. 3(b). As shown in the figure, one long and two short Mn-O bond lengths are found, and while the Mn-O_e-Mn

TABLE II. Room-temperature structural parameters for the rhombohedral ($R\bar{3}c$) phase. Rietveld refinements were carried out using the hexagonal setting of this space group. In this setting the La/Sr atoms reside at (0,0,3/4), the Mn atoms at (0,0,0) and the O atoms at (x,x,1/4). In the case where mixed phases of R and O were observed, occupancies were not refined. The goodness of fit (GoF) agreement index is defined as $R_{wp}/R_{\text{expected}}$.

x	Oc. (La/Sr)	Oc. (Mn)	x[O(1)]	R_{wp}/GoF
$P(O_2)=1.0$ atm				
0.0	0.870(4)	0.974(6)	0.5514(1)	6.1/1.8
0.025	0.892(4)	0.963(5)	0.5525(1)	5.4/1.7
0.075	0.912(4)	0.989(6)	0.5516(1)	6.5/1.7
0.125	0.905(5)	1.02(1)	0.5502(1)	7.7/1.9
0.175	0.902(6)	1.01(1)	0.5476(1)	7.9/2.3
0.225	0.899(6)	1.00(1)	0.5459(2)	8.6/2.7
$P(O_2)=0.195$ atm				
0.0	1.0	1.0	0.5534(5)	6.8/1.6
0.025	1.0	1.0	0.5544(6)	6.8/1.6
0.075	1.0	1.0	0.5529(7)	6.5/1.5
0.125	0.917(7)	1.02(1)	0.5523(2)	7.8/1.6
0.175	0.947(7)	1.01(1)	0.5504(2)	9.2/1.5
0.225	0.898(6)	1.03(1)	0.5479(1)	6.8/2.2
$P(O_2)=9.1\times10^{-3}$ atm				
0.175	1.0	1.0	0.5495(3)	5.7/1.9
0.225	0.929(5)	1.01(1)	0.5476(1)	7.3/2.1
$P(O_2)=1.0\times10^{-3}$ atm				
0.175	1.0	1.0	0.545(1)	9.3/2.6
0.225	0.930(4)	1.01(1)	0.5475(1)	7.0/2.3
$P(O_2)=2.1\times10^{-4}$ atm				
0.175	1.0	1.0	0.5454	7.9/2.7
0.225	0.938(5)	1.05(1)	0.5479(2)	7.8/3.1

TABLE III. Room-temperature structural parameters and cation occupancies for orthohombic ($Pbnm$) phase. In this structure the La/Sr atom resides at (x,y,3/4), the Mn atom at (0,0,0) and the O atoms at (x,y,1/4) and (x,y,z). In the case where mixed phases of R and O were observed, occupancies were set equal to 1 and not refined. The goodness of fit (GoF) agreement index is defined as $R_{wp}/R_{\text{expected}}$.

x	x(La/Sr)	y(La/Sr)	n(La/Sr)	n(Mn)	x[O(1)]	y[O(1)]	x[O(2)]	y[O(2)]	z[O(2)]	R_{wp}/GoF
$P(O_2)=0.195$ atm										
0.0	0.0006(8)	0.5188(6)	1.0	1.0	−0.007(1)	−0.068(1)	0.2306(6)	0.2719(6)	0.0349(3)	6.8/1.9
0.025	0.0024(1)	0.5187(5)	1.0	1.0	−0.0061(9)	−0.0661(8)	0.2309(5)	0.2701(5)	0.03384(3)	6.5/1.5
0.075	0.0016(6)	0.5162(5)	1.0	1.0	−0.0659(8)	−0.0055(9)	0.2315(5)	0.2691(5)	0.0332(3)	9.4/1.4
$P(O_2)=9\times10^{-3}$ atm										
0.0	0.0050(6)	0.5305(4)	0.924(8)	1.02(1)	−0.0689(5)	−0.0052(8)	0.2316(5)	0.2890(5)	0.03410(3)	9.3/4
0.025	0.0061(7)	0.5290(5)	0.930(11)	0.97(2)	−0.0597(8)	−0.0003(8)	0.2160(7)	0.2749(7)	0.0375(3)	11/6.3
0.075	0.0047(5)	0.5263(3)	0.935(7)	1.01(1)	−0.0681(4)	−0.0070(6)	0.2309(5)	0.2843(4)	0.0346(2)	7.5/1.8
0.125	0.0034(5)	0.5175(4)	0.954(6)	1.02(1)	−0.0660(4)	−0.0075(8)	0.2315(4)	0.2713(4)	0.0332(3)	7.6/1.3
0.175	0.0019(7)	0.5203(5)	1.0	1.0	−0.0708(9)	−0.0035(9)	0.2291(6)	0.2671(6)	0.0343(4)	5.7/1.9
$P(O_2)=1.0\times10^{-3}$ atm										
0.125	0.0038(4)	0.5200(3)	0.952(5)	1.01(1)	−0.0677(4)	−0.0056(6)	0.2293(4)	0.2735(4)	0.0329(2)	6.6/1.5
0.175	0.0033(8)	0.5214(6)	1.0	1.0	−0.0689(9)	−0.005(1)	0.2242(8)	0.2684(8)	0.0358(5)	9.3/2.6
$P(O_2)=1\times10^{-4}$ atm										
0.125	0.0028(5)	0.5202(3)	0.951(5)	1.02(1)	−0.0671(5)	−0.0042(7)	0.2272(6)	0.2720(7)	0.0330(2)	7.5/1.7
0.175	−0.003(1)	0.5281(7)	1.0	1.0	−0.080(1)	−0.011(1)	0.235(1)	0.2776(8)	0.0372(7)	8.4/2.6

TABLE IV. Room-temperature structural parameters for monoclinic phase $LaMnO_{3+\delta}$ synthesized at $P(O_2)=2.1\times10^{-4}$ atm. In this structure (space group $P2_1/c$, setting $P12_1/n1$ Mn is located on four special sites: Mn(1)-(0,0,0), Mn(2)-(1/2,0,0), Mn(3)-(0,0,1/2), Mn(4)-(1/2,0,1/2), while the La and O atoms reside on general positions.

Atom	x	y	z
La	0.228 8(9)	0.251 4(20)	0.277 3(9)
La	0.224 5(9)	0.248 9(24)	0.767 9(9)
O(1)	0.270 6(22)	−0.040 2(22)	−0.042 4(24)
O(2)	0.740 0(23)	0.467 7(16)	0.030 8(26)
O(3)	0.038 11(11)	0.252 2(31)	0.036 4(11)
O(4)	0.473 4(10)	0.246 5(26)	−0.048 1(11)
O(5)	0.036 3(27)	−0.041 4(29)	0.238 7(30)
O(6)	0.453 7(26)	0.039 492(29)	0.270 2(27)

angle changes little upon distortion from rhombohedral symmetry, the Mn-O_a-Mn angle is substantially smaller than that observed in the R phase. Full details of the structural parameters for the O phase are listed in Table Va.

The distortion of MnO_6 octahedra associated with the $R\rightarrow O$ phase transition evolving as a function of $P(O_2)$ is given in Fig. 4 for a sample with nominal composition $La_{0.875}Sr_{0.125}MnO_3$. The Mn-O bond length for this composition at $P(O_2)=1.0$ atm is 1.9641(1) Å and increases as $P(O_2)$ decreases. In the O phase, one of the Mn-O_e distances remains essentially unchanged relative to the Mn-O distance in the R phase, while the other two distances Mn-O_a and Mn-O_e' are much larger. The tilt angle between octahedra (Mn-O-Mn) in the R phase is ~163.87(4)° and decreases with $P(O_2)$. In the O phase, the tilt angle between octahedra in the a-b plane is similar to that in the R phase, while the tilt angle parallel to the c axis is substantially smaller (~158°). According to Jonker and van Santen[18] and Wold and Arnott,[19] a critical Mn^{3+}/Mn^{4+} ratio ~25% results in the structural phase transition $R\rightarrow O$ in undoped $LaMnO_{3+\delta}$. The data in Fig. 4 represent a constant $x=0.125$ slice through the x-$P(O_2)$ phase space. The collection of several such slices in the phase diagram of Fig. 1 indicates that the critical Mn^{3+}/Mn^{4+} ratio occurs for 9.1×10^{-3} atm$<P(O_2)<$0.195 atm with $x\leqslant0.175$. For $x>0.175$, a sufficient concentration of Mn^{3+} to induce the phase transition cannot be obtained in the $P(O_2)$ regime studied; the rhombohedral phase is always stable.

The monoclinic polymorph of $La_{1-x}Sr_xMnO_{3+\delta}$ has previously been observed by Yakel[17] and Wollan and Koehler,[24] but its crystal structure has not yet been described in detail. X-ray-diffraction patterns taken of samples in the monoclinic stability region of Fig. 1 are in qualitative agreement with diffraction data for stoichiometric $LaMnO_3$ reported by Takeda *et al.*[25] However, these researchers indexed the observed diffraction pattern on an orthorhombic cell ($\sqrt{2}a_p\times\sqrt{2}a_p\times2c_p$, where a_p, b_p, and c_p are the ideal cubic perovskite axes). Earlier, Yakel[17] reported that a nearly stoichiometric sample of $LaMnO_3$ crystallized in a monoclinic cell with dimensions $2a_p\times2b_p\times2c_p$. Indexing of both x-ray and neutron-diffraction patterns from our samples was consistent with this monoclinic cell. In fact, lattice parameters determined from our $LaMnO_{3+\delta}$ sample [$P(O_2)=2.1\times10^{-4}$ atm] agree well with those reported by Yakel[17] [this work: $a=7.9670(5)$ Å, $b=7.7000(2)$ Å, $c=7.9564(5)$ Å, $\beta=91.884(2)°$; Yakel: $a=7.960$ Å, $b=7.698$ Å, $c=7.960$ Å, $\beta=91.87°$]. Observed reflections are consistent with three monoclinic space groups: $P2/c$, $P2_1/c$, and $P2_1/m$. Least-squares refinement of neutron powder data using models based on these three space groups indicates that a structural model using space group $P2_1/c$ provides the best fit to the observed diffraction pattern [$R_{wp}=6.7\%$, $R(F^2)=3.5\%$], while models using the other space groups fail to converge to a satisfactory solution. The refined structural parameters for the representative monoclinic sample $LaMnO_{3+\delta}$, are given in Table IV and Mn-O bond lengths and Mn-O-Mn bond angles, are given in Table V(b). These parameters are little changed in the doped monoclinic samples.

According to Takeda, the monoclinic polymorph of $LaMnO_{3+\delta}$ (which he indexed as orthorhombic) occurs for samples with full cation stoichiometry,[25] indicating that the

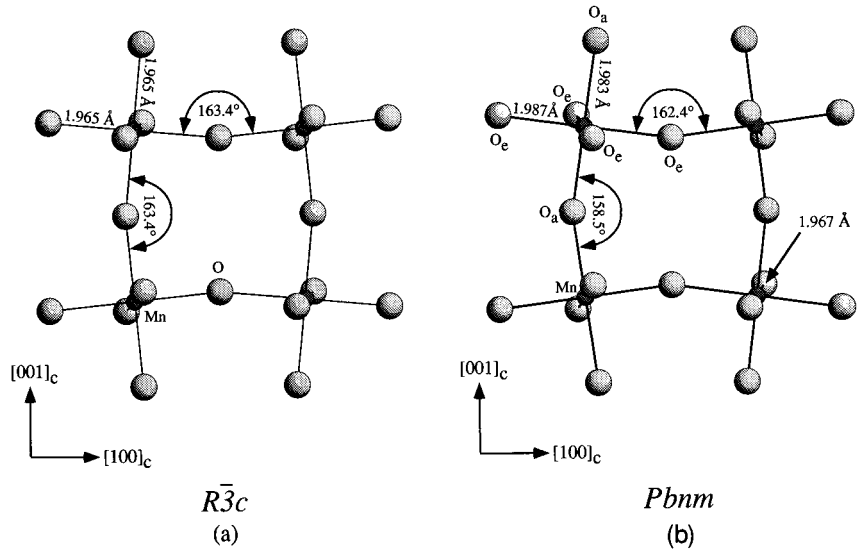

FIG. 3. Sections along the cubic (010) plane for both the (a) rhombohedral and (b) orthorhombic structures.

TABLE V. (a) Mn-O bond lengths and Mn-O-Mn bond angles for the rhombohedral and orthorhombic phases. (b) Mn-O bond lengths and Mn-O-Mn bond angles for the monoclinic phase $LaMnO_{3+\delta}$ synthesized at $P(O_2)=2.1\times10^{-4}$ atm.

(a)

	Rhombohedral		Orthorhombic				
x	Mn-O	Mn-O-Mn	Mn-O_a	Mn-O_{e1}	Mn-O_{e2}	Mn-O_a-Mn	Mn-O_e-Mn
$P(O_2)=1$ atm							
0	1.9648(1)	163.39(4)					
0.025	1.9660(1)	163.06(4)					
0.075	1.9660(1)	163.32(4)					
0.125	1.9638(1)	163.87(4)					
0.175	1.9610(1)	164.59(5)					
0.225	1.9595(1)	165.24(6)					
$P(O_2)=0.195$ atm							
0	1.9693(4)	162.7(2)	1.984(1)	1.985(4)	1.968(4)	158.0(3)	161.6(2)
0.025	1.9704(5)	162.5(2)	1.9816(9)	1.976(3)	1.972(3)	158.5(3)	162.2(1)
0.075	1.9692(6)	162.9(2)	1.9799(8)	1.974(3)	1.972(3)	158.7(3)	162.7(1)
0.125	1.9686(1)	163.10(6)					
0.175	1.9661(1)	163.72(5)					
0.225	1.9631(1)	164.58(5)					
$P(O_2)=9.1\times10^{-3}$ atm							
0			1.9764(6)	1.916(3)	2.079(3)	157.6(2)	159.9(1)
0.025			1.9706(8)	1.967(5)	2.032(5)	160.0(3)	158.8(2)
0.075			1.9794(5)	1.932(3)	2.051(3)	157.9(1)	160.3(1)
0.125			1.9827(5)	1.987(3)	1.967(3)	158.6(2)	162.4(1)
0.175	1.9672(2)	164.98(8)	1.986(3)	1.961(4)	1.992(4)	157.2(3)	162.2(2)
0.225	1.9621(1)	164.7(4)					
$P(O_2)=1.0\times10^{-3}$ atm							
0.125			1.9846(4)	1.989(3)	1.969(3)	158.1(1)	162.0(1)
0.175	1.9633(7)	165.5(1)	1.984(1)	1.952(5)	2.011(5)	157.7(3)	160.9(2)
0.225	1.9623(1)	164.69(4)					
$P(O_2)=2.1\times10^{-4}$ atm							
0.125			1.9834(5)	1.974(4)	1.986(4)	158.4(2)	162.0(1)
0.175	1.9614(4)	165.3(7)	1.996(1)	1.938(7)	2.035(7)	154.0(3)	160.6(3)
0.225	1.9640(1)	164.59(5)					

(b)

Mn(1)-O(1)	2.215(19)	Mn(2)-O(1)	1.873(17)
Mn(1)-O(3)	1.985(24)	Mn(2)-O(4)	1.944(20)
Mn(1)-O(5)	1.938(21)	Mn(2)-O(6)	2.214(26)
Mn(3)-O(2)	1.936(18)	Mn(4)-O(2)	2.108(20)
Mn(3)-O(4)	2.001(20)	Mn(4)-O(3)	1.952(24)
Mn(3)-O(5)	2.133(28)	Mn(4)-O(6)	1.877(18)
Mn(1)-O(3)-Mn(4)	155.8(5)	Mn(2)-O(4)-Mn(3)	154.8(5)
Mn(4)-O(6)-Mn(2)	153.0(2)	Mn(3)-O(5)-Mn(1)	155.5(2)
Mn(1)-O(1)-Mn(2)	153.9(9)	Mn(3)-O(2)-Mn(4)	160.1(9)
Mn(2)-O(4)-Mn(3)	154.8(5)	Mn(4)-O(3)-Mn(1)	155.8(5)

valence state of Mn is formally +3 in these samples. Thus, we again expect the MnO_6 octahedra of monoclinic samples to be Jahn-Teller distorted. The solution of this structure for a sample of $LaMnO_{3+\delta}$ synthesized at $P(O_2)=2.1\times10^{-4}$ atm indicates that there are four symmetry-independent Mn sites and four symmetry-independent MnO_6 octahedra of different sizes. Two projections of this structure are shown in Fig. 5. Each MnO_6 octahedra has three different Mn-O bond lengths ranging from 1.873 to 2.215 Å. The tilt angle between octahedra varies from 154.8(5)° to 160.1(9)°. As a result of the

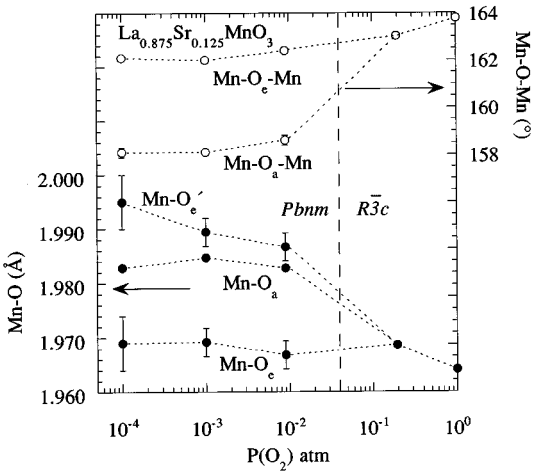

FIG. 4. Variations of Mn-O bond lengths and Mn-O-Mn bond angles as a function of $P(O_2)$ for $La_{0.875}Sr_{0.125}MnO_{3+\delta}$.

tilting and distortion of octahedra, the La atom is also displaced relative to its ideal site, forming La-O bonds ranging from 2.4 to 2.6 Å.

The defect chemistry of $La_{1-x}Sr_xMnO_{3+\delta}$ is similar to that reported for $LaMnO_{3+\delta}$. Refinement of site occupancies agrees with the proposition that these manganites form cation rather than oxygen vacancies.[8,13–15] Van Roosmalen and Cordfunke[13] have proposed that for $LaMnO_{3+\delta}$ vacancies occur in equal numbers for both the *A* and *B* site cations, i.e., $La_{1-y}Mn_{1-y}O_3$. However, our refinements consistently yield a higher concentration of vacancies on the La/Sr site than on the Mn site (see Tables II and III). The highest cation vacancy concentrations are observed for samples prepared under $P(O_2) \geq 0.195$ atm, while progressively more stoichiometric samples are obtained from preparations at lower $P(O_2)$. Increasing Sr doping in the single-phase rhombohedral samples [$P(O_2)=1.0$ atm] results in a progressive increase in both *A*- and *B*-site occupancies, saturating at $x \sim 0.125$. Interestingly, in the orthorhombic samples [e.g., $P(O_2)=9.0\times10^{-3}$ atm], the Mn site is fully occupied for all measured doping levels, while the La/Sr site becomes increasingly occupied with greater doping. We note that the refined occupancies of *R*-phase samples indicate that for $P(O_2)>0.195$ atm, metal vacancy concentrations are on the order of 10% or greater. Charge balance is achieved in these cation-deficient samples by a portion of Mn ions increasing their valence state from +3 to +4. For samples synthesized at $P(O_2)<0.195$ atm a lesser concentration of cation vacancies is found, indicating an increased Mn^{3+}/Mn^{4+} relative to those samples synthesized at higher $P(O_2)$. This increase in Mn^{3+} concentration correlates with the observation of the Jahn-Teller distortion in the orthorhombic and monoclinic phases, both synthesized under conditions of low $P(O_2)$.

IV. MAGNETIC AND ELECTRONIC TRANSPORT PROPERTIES

Magnetization and susceptibility measurements indicate that samples with $x \geq 0.125$ are ferromagnetic (Fig. 6), while those with $x<0.125$ are antiferromagnetic (Fig. 7), in agreement with Urushibara *et al.*[4] Figure 6 shows that in crossing the *R-O* phase boundary with increasing *x*, no qualitative change in the magnetization is observed, so that ferromagnetism is not associated with a unique crystal symmetry. Magnetization vs temperature for these samples shows a significant high-temperature tail; thus, we have used the procedure adopted by Urushibara *et al.*,[4] to operationally define T_C as the inflection point in the susceptibility curves (Fig. 8). These T_C values increase with Sr doping. Unique to the present investigation, however, is the effect of $P(O_2)$ on T_C, shown in Fig. 8(b). Contrary to the results of Schiffer *et al.*[20] for (La,Ca)MnO_3, we find a marked dependence of T_C on $P(O_2)$—and hence cation vacancy concentration—in the $La_{1-x}Sr_xMnO_{3+\delta}$ system.

The phase diagram of Fig. 1 divides the structural properties of $La_{1-x}Sr_xMnO_{3+\delta}$ as a function of *x* and $P(O_2)$; this same figure also differentiates the electronic transport properties of the samples lying in this region of phase space. The resistivity versus temperature is shown in Fig. 9 for representative rhombohedral and orthorhombic samples. As can be seen in Fig. 9(a), Sr-doped *R*-phase samples display a broad maximum in ρ vs *T*. Above this maximum, samples of the *R* phase display a negative temperature coefficient of resistance, suggesting that the phase is semiconducting in

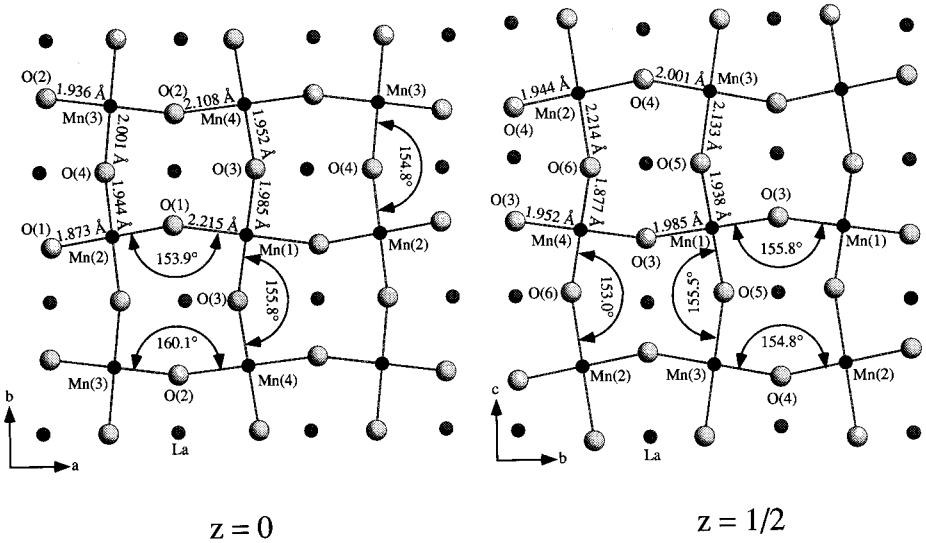

FIG. 5. Projections of the monoclinic structure of $LaMnO_{3+\delta}$ synthesized at $P(O_2)=2.1\times10^{-4}$ atm perpendicular to (a) the *c* axis and (b) the *a* axis.

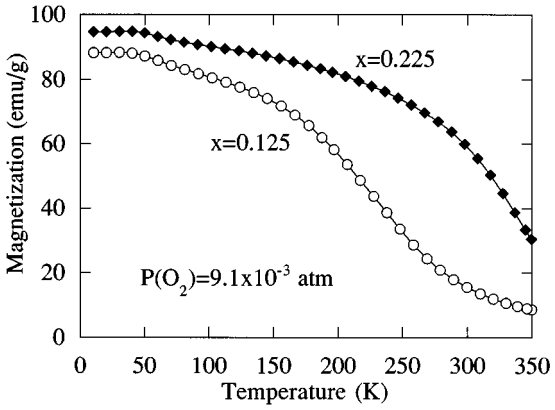

FIG. 6. Magnetization in a 5 T applied field for rhombohedral ($x=0.225$) and orthorhombic ($x=0.125$) samples.

this temperature regime. The metal-insulator (M-I) transition indicated by the resistivity data for our R-phase samples is much broader than that of related compounds published by others.[4,26,27] We believe that the sharpness of this transition is perhaps the most severe test of sample quality and that the broad transitions suggest a degree of compositional inhomogeneity in our samples. This inhomogeneity could result from the low synthesis temperature used in this study (1000 °C) or from the fact that we used only one mixing and firing sequence. Both of these are in contrast to some other researchers who have used higher temperatures ($\geqslant$1300 °C) and repeated grinding and refiring to improve sample homogeneity. For the large number of compositions studied here, such a tedious synthesis procedure was not practical. The broadening of the metal-insulator transition prevents us from attempting to correlating the M-I transition with T_C or with particular structural phenomena. Importantly, however, the inhomogeneity is not large enough to result in broadening of the diffraction peaks. Thus, the correlation of the magnetic and transport behavior to regions of the structural phase diagram (Fig. 1) is clear. Figure 9(b) shows that independent of x or $P(O_2)$, the O phase is nonmetallic between 20 and 350 K. As shown in Fig. 10(c) the M phase shows resistive behavior similar to that of the O phase, as both of these structures are Jahn-Teller distorted.

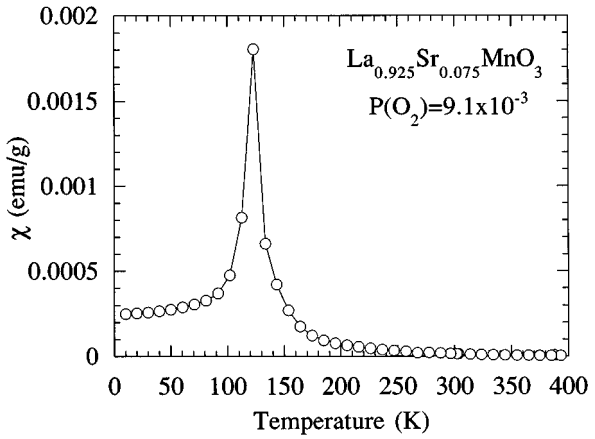

FIG. 7. Magnetic susceptibility of monoclinic $La_{0.925}Sr_{0.075}MnO_{3+\delta}$ synthesized at $P(O_2)=1.0\times10^{-3}$ atm as a function of temperature.

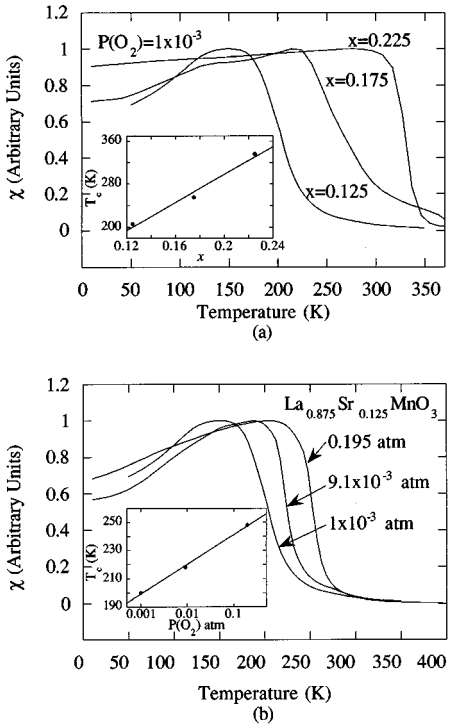

FIG. 8. (a) Magnetic susceptibility as a function of temperature and x for $P(O_2)=1.0\times10^{-3}$ atm (b) Magnetic susceptibility as a function of temperature and synthesis $P(O_2)$ for $x=0.125$.

Both nonmetallic and metallic samples show a magnetoresistance effect. Table VI shows that when expressed as a ratio, i.e., $\Delta\rho/\rho_{9T}$ [where $\Delta\rho=(\rho_0-\rho_{9T})$], the maximum magnetoresistance for each member of the series of samples—regardless of crystal symmetry—lies between 92 and 230 %, with a trend toward greater $\Delta\rho/\rho_{9T}$ with decreasing x. No clear trend is apparent as a function of $P(O_2)$. These values are somewhat deceptive since $\Delta\rho$ for the nonmetallic samples are slightly larger than those reported for the million-fold MR ratio by Gong *et al.*,[6] but ρ_{9T} of these samples is orders of magnitude larger than that of the metallic samples. Figure 10 shows plots of ρ and $\Delta\rho$ for a metallic rhombohedral sample [$x=0.225$, $P(O_2)=0.195$ atm], a nonmetallic orthorhombic sample [$x=0.125$, $P(O_2)=9.1\times10^{-3}$ atm], and a nonmetallic monoclinic sample [$x=0.075$, $P(O_2)=1.0\times10^{-3}$ atm]. Scanning electron microscopy reveals a small grain size ($\sim$0.5 μm) for the measured samples, and low-current I-V characteristics show evidence of intergrain tunneling. Therefore, a large ρ_{9T} in the metallic samples is not particularly surprising and may be the cause for the relatively modest magnetoresistance ratios in these samples. As can be seen from the figure, $\Delta\rho$ for the metallic (R phase) sample is about $\sim$0.11 Ω cm, while that of the nonmetallic (O phase and M phase) samples is $\sim10^4$ Ω cm at low temperature. Both of these $\Delta\rho$ values are comparable to the highest reported thus far.[6]

It should be noted that the low temperature values of $\Delta\rho$ for the metallic samples are substantially larger than has been reported for single-crystal samples of similar composition.[4] The origin of this difference ($\Delta\rho\sim50$ mΩ cm compared to $\sim$1 mΩ cm in Ref. 4) is unclear but may be a

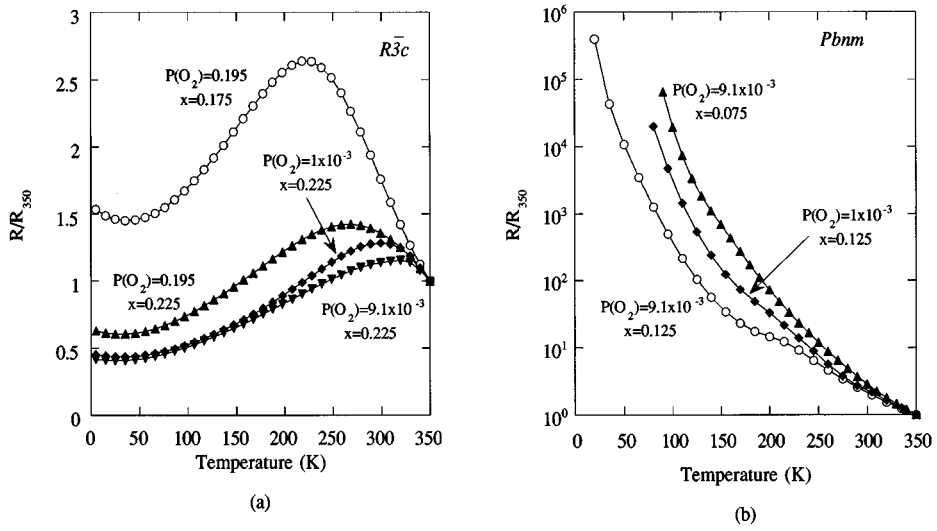

FIG. 9. (a) Resistivity for a number of rhombohedral samples and (b) orthorhombic samples. The samples whose resistivity is shown here are marked in Fig. 1 by a †.

consequence of magnetic domain size and the overall softness of the ferromagnetic state. In the case of large single crystals, the domains will grow to a size dictated only by sample dimensions (i.e., domain size ≫ scattering length). However, in our polycrystalline samples, the small grain size and possible chemical inhomogeneity may result in the formation of microdomains whose length scale is sufficiently small to affect the scattering of charge carriers (i.e., domain size ~ scattering length). Further work on the micromagnetics of these systems will be needed to clarify this question.

V. DISCUSSION

The present work shows that synthesis $P(O_2)$ has a dramatic effect on the structural, magnetic, and transport properties in $La_{1-x}Sr_xMnO_{3+\delta}$. Structurally, $P(O_2)$ produces structural phase transitions between rhombohedral and orthorhombic or orthorhombic and monoclinic phases as a result of changes in the cation vacancy concentration. It also has a marked effect on the magnetism, shifting T_C over a wide range in the $P(O_2)$ regime studied. $P(O_2)$ can also modify the electronic transport properties of the materials, delineating an electronic phase boundary between a metal and a nonmetal. Finally, $P(O_2)$ can affect the coupling between magnetism and transport, i.e., the double exchange of electrons between ferromagnetically coupled Mn ions. We see this effect dramatically in the orthorhombic materials, where the nonmetal-to-metal transition seen in the rhombohedral samples disappears.

The effect of $P(O_2)$ on T_C is of some significance in light of reports to the contrary in related systems. Schiffer *et al.*[20] have reported that T_C for $(La,Ca)MnO_{3+\delta}$ is insensitive to the synthesis atmosphere. Our results in the $La_{1-x}Sr_xMnO_{3+\delta}$ system are rather different; we see a variation of ~50 K in T_C over two decades of increasing $P(O_2)$ for an $x=0.125$ sample [Fig. 9(b)]. As our neutron-diffraction data show, increasing $P(O_2)$ results in samples with a higher cation vacancy concentration, and hence a smaller Mn^{3+}/Mn^{4+} ratio. This ratio also decreases with increasing Sr doping, x. T_C is observed to increase with increasing x [Fig. 9(a)]. The variation of T_C with $P(O_2)$ is thus consistent with the variation of T_C with x and is almost certainly related to the Mn^{3+}/Mn^{4+} ratio.

Torrance, Lacorre, and Nazzal[29] have shown for the $RNiO_3$ perovskites that changes in the Ni-O-Ni angle, α, have a substantial effect on the electronic transport, an effect he attributes to a modification of the d-electron bandwidth as

TABLE VI. Maximum $\Delta\rho/\rho_{9T}$ (%) as a function of x and $P(O_2)$ for $La_{1-x}Sr_xMnO_{3+\delta}$.

	x in $La_{1-x}Sr_xMnO_{3+\delta}$			
$P(O_2)$	0.075	0.125	0.175	0.225
0.195 atm		212	104	100
9.1×10^{-3} atm	186	186		100
1.0×10^{-3} atm	222	230	144	92

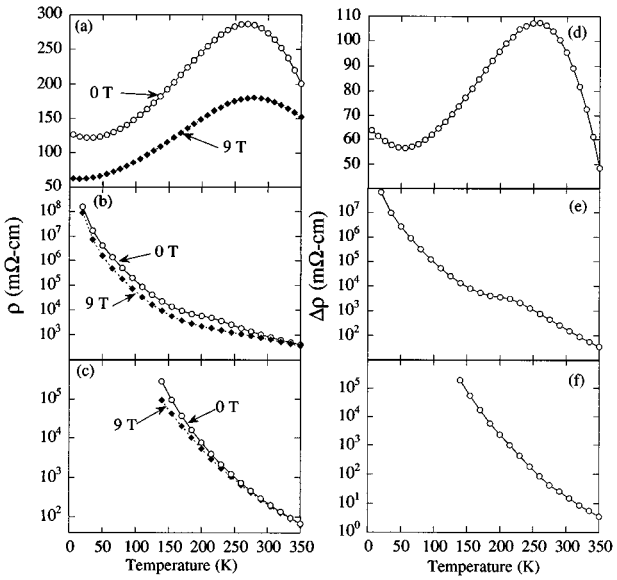

FIG. 10. Resistivity at 0 and 9 T for (a) rhombohedral [$x=0.225$, $P(O_2)=0.195$ atm], (b) orthorhombic [$x=0.125$, $P(O_2)=9.1\times10^{-3}$ atm], and (c) monoclinic samples [$x=0.075$, $P(O_2)=1.0\times10^{-3}$ atm). $\Delta\rho$ as a function of temperature is shown in (d), (e), and (f) for the respective samples.

a function of α. Smaller values of α result in a narrow bandwidth and a charge-transfer insulator; larger values result in wider bandwidth and a metal. We see a similar effect in $La_{1-x}Sr_xMnO_{3+\delta}$: large Mn-O-Mn angles in the rhombohedral phase ($\sim$163°) result in a metallic state, while small angles ($\sim$157°) characterize the nonmetallic orthorhombic phase. However, this connection between structure and transport is purely electronic, with no coupling to the magnetism.

Further, we have noted in Fig. 4 that the Mn-O_a-Mn changes with $P(O_2)$, while the equatorial Mn-O_e-Mn angles remain essentially unchanged as the *R-O* phase boundary is crossed. This indicates a possible source of anisotropy in the transport properties of the materials, an anisotropy induced by the structural phase transition. As the Mn-O_e-Mn angle is essentially the same as that of the metallic rhombohedral phase, one can speculate that transport parallel to the orthorhombic *a-b* plane will be significantly greater than that parallel to the *c* axis. A single-crystal measurement will be required to test this hypothesis.

According to the double exchange model, the electron hopping matrix element *b* is proportional to $\cos(\theta/2)$, where θ is the angle between adjacent Mn moments.[30] Because the direction of the Mn moment relative to the axes of the MnO_6 octahedron is determined in large part by the crystal field, it is expected that θ will depend on the Mn-O-Mn tilt angle α described above. Hwang *et al.*[28] have demonstrated that by modifying the effective ionic size of the *A*-site cation (La/Sr site) they could vary α. As an alternative to *A*-site substitutions, α can be modified by synthesis $P(O_2)$, deviating dramatically from its value in the metallic *R* phase as the *R-O* phase boundary is crossed with decreasing $P(O_2)$ (Fig. 4). Thus, the angle θ also is expected to vary with $P(O_2)$. Such a variation may explain why the orthorhombic and monoclinic materials do not exhibit the ferromagnetically induced metal-insulator transition observed in the rhombohedral samples.

The transport properties of the samples studied indicate that in the (LaSr) MnO_3 system the structural phase diagram and the metal-insulator transition are linked. The metal-to-nonmetal transition is observed only in our rhombohedral samples; a similar result was reported by Urushibara *et al.*[4] in this system. In contrast, Hwang *et al.*[28] report that orthorhombic $La_{0.525}Pr_{0.175}Ca_{0.3}MnO_3$ undergoes a metal-insulator transition with $T_C \sim 210$ K. It is interesting to note that the distortion of the MnO_6 octahedra in Hwang's sample is quite small (Mn-O_{ax}=1.966 Å; Mn-O_{eq}=1.979 Å, 1.951 , while the distortions in our orthorhombic and monoclinic samples are typically much larger [see Tables V(a) and VI(b)]. This difference may be responsible for the different transport behaviors observed between Hwang's and our orthorhombic samples.

Transport measurements demonstrate that MR effects are present below T_C in all samples. The largest effects are seen in the orthorhombic phase. Although the change in resistivity is comparable to what others have reported, the *O*-phase samples never become metallic, and so the percentage change in resistivity for these samples is only moderate.

VI. CONCLUSIONS

The structural phase diagram of $La_{1-x}Sr_xMnO_{3+\delta}$ has been constructed as a function of both Sr doping ($0 \leqslant x \leqslant 0.225$) and oxygen partial pressure during synthesis (2.1×10^{-4} atm$\leqslant P(O_2) \leqslant 1$ atm). Three distinct crystallographic phases (*R*, *O*, and *M*) form in this region of phase space. The low-temperature ground state of the rhombohedral phase is a ferromagnet for all *x* and $P(O_2)$ in the studied range, while the monoclinic phase is antiferromagnetic in its region of stability. The orthorhombic phase is ferromagnetic for $x \geqslant 0.125$. Transport measurements show that the rhombohedral samples exhibit a metal-insulator transition at temperatures close to the Curie temperature but that the orthorhombic and monoclinic samples remain nonmetallic throughout the temperature range studied. We have shown that synthesis $P(O_2)$ can have a dramatic effect on the structural, magnetic, and transport properties of the $La_{1-x}Sr_xMnO_{3+\delta}$ samples. That these effects can impact those induced by Sr doping implies that $P(O_2)$ may be a significant process variable in the design and synthesis of new magnetoresistive oxides.

ACKNOWLEDGMENTS

The authors thank Simine Short for invaluable assistance in the powder neutron-diffraction measurements. This work was supported by the U.S. Department of Energy Distinguished Postdoctoral Research Program sponsored by the U.S. Department of Energy, Office of Science Education and Technical Information, and administrated by the Oak Ridge National Laboratory (J.F.M.), by the NSF Office of Science and Technology Centers under Contract No. DMR 91-20000 (D.N.A.), and by the U.S. Department of Energy, Basic Energy Sciences-Materials Sciences and ER-LTT, under Contract No. W-31-109-ENG-38 (C.D.P. D.G.H., J.D.J., and S.D.B.).

*Corresponding author.

†Also with Science and Technology Center for Superconductivity, Argonne National Laboratory, Argonne, IL 60439.

[1] R. van Helmolt, J. Wecker, B. Holzapfel, L. Schultz, and K. Samwer, Phys. Rev. Lett. **71**, 2331 (1993).

[2] M. McCormack, S. Jin, T. H. Tiefel, R. M. Fleming, J. M. Phillips, and R. Ramesh, Appl. Phys. Lett. **64**, 3045 (1994).

[3] S. S. Manoharan, N. Y. Vasanthacharya, M. S. Hegde, K. M. Satyalakshmi, V. Prasad, and S. V. Subramanyam, J. Appl. Phys. **76**, 3923 (1994).

[4] A. Urushibara, Y. Moritomo, T. Arima, A. Asamitsu, G. Kido, and Y. Tokura, Phys. Rev. B. **51**, 14 103 (1995).

[5] A. Asamitsu, Y. Moritomo, Y. Tomioka, T. Arima, and Y. Tokura, Nature (London) **373**, 407 (1995).

[6] G.-Q. Gong, C. Canedy, G. Xiao, J. Z. Sun, A. Gupta, and W. J. Gallagher, Appl. Phys. Lett. **67**, 1783 (1995).

[7] V. Caignaert, A. Maignan, and B. Raveau, Solid State Commun. **95**, 357 (1995).

[8] J. A. M. van Roosmalen, E. H. P. Cordfunke, R. B. Helmholdt, and H. W. Zandbergen, J. Solid State Chem. **110**, 100 (1994).

[9] P. G. deGennes, Phys. Rev. **118**, 141 (1960).

[10] J. B. Goodenough, Phys. Rev. **100**, 564 (1955).

[11] A. J. Millis, P. B. Littlewood, and B. I. Shraiman, Phys. Rev. Lett. **74**, 5144 (1995).

[12] W. E. Pickett and D. J. Singh, Phys. Rev. B (to be published).
[13] J. A. M. van Roosmalen and E. H. P. Cordfunke, J. Solid State Chem. **110**, 106 (1994).
[14] J. A. M. van Roosmalen and E. H. P. Cordfunke, J. Solid State Chem. **110**, 109 (1994).
[15] J. A. M. van Roosmalen, P. van Vlaanderen, and E. H. P. Cordfunke, J. Solid State Chem. **114**, 516 (1995).
[16] J. B. A. A. Elemans, B. van Laar, K. R. van den Veen, and B. O. Loopstra, J. Solid State Chem. **3**, 238 (1971).
[17] H. L. Yakel, Jr., Acta Crystallogr. **8**, 394 (1955).
[18] G. H. Jonker and J. H. van Santen, Physica **16**, 337 (1950).
[19] A. Wold and R. J. Arnott, J. Phys. Chem. Solids **9**, 176 (1959).
[20] P. Schiffer, A. P. Ramirez, W. Bao, and S.-W. Cheong, Phys. Rev. Lett. **75**, 3336 (1995).
[21] J. D. Jorgensen, J. J. Faber, J. M. Carpenter, R. K. Crawford, J. R. Haumann, R. L. Hitterman, R. Kleb, G. E. Ostrowski, F. J. Rotella, and T. G. Worton, J. Appl. Crystallogr. **22**, 321 (1989).
[22] A. C. Larson and R. B. Von Dreele, General Structure Analysis System, Los Alamos Internal Report No. 86-748 (1985–1990).
[23] L. J. Van der Pauw, Phillips Res. Rep. **13**, 334 (1958).
[24] E. O. Wollan and W. C. Koehler, Phys. Rev. **100**, 545 (1955).
[25] Y. Takeda, S. Nakai, R. Kanno, N. Imanishi, G. Q. Shen, and O. Yamamoto, Mater. Res. Bull. **26**, 153 (1991).
[26] Y. Tokura, A. Urushibara, Y. Moritomo, T. Arima, A. Asamitsu, G. Kido, and N. Furukawa, J. Phys. Soc. Jpn. **63**, 3931 (1994).
[27] Y. Tomioka, A. Asamitsu, Y. Moritomo, and Y. Tokura, J. Phys. Soc. Jpn. **64**, 3626 (1995).
[28] H. Y. Hwang, S.-W. Cheong, P. G. Radaelli, M. Marezio, and B. Batlogg, Phys. Rev. Lett. **75**, 914 (1995).
[29] J. B. Torrance, P. Lacorre, and A. I. Nazzal, Phys. Rev. B **45** 8209 (1992).
[30] P. W. Anderson and H. Hasegawa, Phys. Rev. **100**, 675 (1955).